Multistatic MIMO Sparse Imaging Based on FFT and Low Rank Matrix Recovery Techniques

Shaoqing Hu, *Member, IEEE,* Amir Masoud Molaei, Okan Yurduseven, *Senior Member, IEEE,* Hongying Meng, *Senior Member, IEEE,* Rajagopal Nilavalan, *Senior Member, IEEE,* Lu Gan, *Senior Member, IEEE,* Xiaodong Chen, *Fellow, IEEE*

***Abstract*—This paper proposes a simple sparse imaging scheme of using a linear sparse aperiodic array and a new fast Fourier transform (FFT) matched filtering algorithm for a THz multistatic multiple-input and multiple-output (MIMO) imaging system. The simple linear sparse aperiodic array and mutlipass interferometric synthetic aperture focusing technique are used to achieve a fast sampling, low system cost and high imaging performance. Unlike a traditional generalized synthetic aperture focusing technique (GSAFT) for multistatic MIMO imaging, which is time consuming and exhibits increased reconstruction time with increased data volume, the proposed FFT matched filtering (FFTMF) image reconstruction algorithm is capable of providing comparable image quality but significantly reducing the reconstruction time. For example, we show that for an image of 300 mm $\times$ 320 mm with a pixel size of 0.75 mm $\times$ 0.83 mm, the reconstruction time is reduced from about 1.50 minutes to 0.25 s in the 220 GHz 5-pass synthetic imaging experiments. The proposed imaging algorithm uses an internal zero padding, a multipass interferometric synthetic aperture focusing technique and a wideband imaging technique to improve the imaging performance under a low-cost, sparse sampling scheme. It shows a strong anti-noise ability and a high tolerance to target focusing distance. In addition, integrated with a algorithm of principal component pursuit by alternating directions method (PCPADM), sparse imaging is available to further save system cost and sampling data without a loss of image quality while the novel use of error matrix provides an additional detection capability for imaging systems.**

***Index Terms*—3D Fast Fourier transform matched filtering, GSAFT, low rank matrix recovery (LRMR), MIMO, PCPADM, sparse synthetic aperture imaging, sparse periodic array (SPA).**

I. Introduction

MICROWAVE up to Terahertz (THz) imaging has been greatly improved in last two decades for radar, sensing, personnel screening/security detection and non-destructive testing [1]–[5]. There is of great significance to conduct personnel screening in public areas such as airport, train stations and gathering buildings. Imaging systems fall into different categories if using different categorizing methods, for example, passive imaging system [6], active imaging system [7], Quasi-optical imaging system [8], continuous wave system [9], synthetic aperture radar (SAR) system [10], [11], linear and planar array electronic scanning imaging system [11]–[16]. These categories are not excluded and one imaging system may fall into two or more categories because of its working principle or scanning approach. Active imaging systems leveraging the synthetic aperture focusing technique is superior on image signal-to-noise ratio and exhibit high image contrast compared to passive ones. The drawback of long sampling time resulting from the need to scan large aperture area can be potentially solved by electronic scanning of an array in which the transmitters are sequentially turned on by electronic switches in microseconds, and all the receivers record the echoes at the same time. However, traditional monosatic uniform arrays and most multistatic uniform/sparse MIMO arrays use sampling spacing on the order of $\lambda/2$ or being released to λ in practice by Nyquist sampling criterion to avoid aliasing. This will increase the data acquisition time due to a large number of sampling points required and system cost because of consequent channels especially at millimeter-wave (mm-wave) and THz bands. For example, there are a total of 736 transmitter (Tx) antennas and 736 receiver (Rx) antennas used in a planar imaging system working at 72-80 GHz [15]. We have investigated the feasibility of using a linear sparse periodic array (SPA) with large sampling spacing for 220 GHz imaging and applied a multipass interferometric synthetic aperture focusing technique to improve image quality for detecting more challenging targets without increasing hardware complexity [17]. The demonstrated imaging performance with a low cost system setup is promising to security target detection and non-destructive testing. However, the image reconstruction based on GSAFT is time consuming because of iterative superposition. Moreover, the multistatic MIMO topology of the SPA makes it impossible to apply fast Fourier transform (FFT)-based reconstruction techniques. Although there are some researches on FFT-based multistatic MIMO imaging, they mainly focus on low frequency bands, dense sampling, single-pass synthetic aperture scanning, uniform MIMO arrays [11]–[16], [18], [19]. Therefore, in this paper a novel multipass synthetic aperture imaging algorithm based on FFT matched filtering technique compatible with multistatic MIMO setups (SPA used in experiments) is proposed for THz sparse imaging. Compared to conventional FFT matched filtering approach, the internal padding of zeros is proposed to achieve a denser image pixel and improved image quality so the large sampling spacing or fewer array elements can be used [16], [20], [21]. The multipass interferometric imaging

The work is funded by Brunel University London under Research Development Fund (RDF) LBG194 and Brunel Research Initiative and Enterprise Fund (BRIEF) 2022/2023 Award 12455. The work of O. Yurduseven and A.M. Molaei was funded by the Leverhulme Trust under Research Leadership Award RL-2019-019.

Shaoqing Hu, Hongying Meng, Rajagopal Nilavalan and Lu Gan are with Department of Electronic and Electrical Engineering, College of Engineering, Design & Physical Sciences, Brunel University London, Uxbridge, UB8 3PH, UK (e-mail: shaoqing.hu@brunel.ac.uk).

Amir Masoud Molaei and Okan Yurduseven are with Institute of Electronics, Communications and Information Technology, Queen's University Belfast, Belfast, BT3 9DT, UK.

Xiaodong Chen is with School of Electronic Science and Computer Science, Queen Mary University of London, London, E1 4NS, UK.

technique is incorporated to improve image quality but it does not increase the hardware complexity of system. With the proposed FFT-based imaging approach the image reconstruction time reduces significantly and it becomes independent to data volume. Furthermore, wideband imaging operation can be used to achieve a range resolution and reconstruct 3D target images of the scene [22]. The proposed FFT-based 3D image reconstruction approach is time efficient compared to wavenumber domain algorithms without need of a stolt interpolation of wavenumbers in spatial frequency domain and the performance including the sparse imaging has been successfully verified with simulated data [23], [24].

Sparse imaging including compressive sensing is a promising technique to break the Nyquist sampling condition. This reduces the sampling time and system cost in particular [21], [25], [26]. In order to apply sparse imaging, two key conditions should be fulfilled. One is a hardware implementation like sparse arrays to achieve a sparse sampling pattern, and the other one is an effective algorithm to recover the data. In this regard, random binary matrices are widely used to generate a sparse sampling pattern in simulation studies of sparse imaging (compressive sensing). However, there is very little research about how to design a sparse sampling pattern, not to mention the practical implementation because of complexity. A 2D pseudorandom spiral-sampling pattern for sparse imaging is proposed for a monostatic configuration while one transceiver with a raster scanning scheme is used in the experiments [27]. One 2D SPA and two 2D sparse aperiodic arrays, which are multistatic configurations, are proposed for near-field UWB imaging in [28]. However, the synthesized 2D virtual arrays are not suitable for large aperture sampling and image reconstruction approach based on modified Kirchhoff migartion is too complex. In this paper a simple designed linear sparse aperiodic array is used for random sparse sampling.

Regarding the target image reconstruction in sparse imaging, the algorithm based on low rank matrix recovery (LRMR) technique with principal component pursuit by alternating directions method (PCPADM) has been investigated in this paper. Compared to emergent deep learning based image reconstruction approach, image reconstructions based on low rank matrix completion (LRMC) or LRMR exempt from training stage with use of large amount of data [29]–[31]. Moreover, the network is only valid for one specific imaging model after trained [31]. Compared to random sparse imaging based on compressive sensing (CS), LRMC or LRMR using the low-rank constraint is superior because of its robustness against basis-mismatch, lower demand on computing resources and simplicity of exempting from the sparse representation [27], [32]–[34]. LRMC has gained significant interest in various applications such as W-band 0.4m-SAR imaging for target detection [27], remote SAR imaging [35], [36] and multipass interferometric synthetic aperture imaging at 220 GHz for detecting a more challenging target at 1.4 m [17]. Different from LRMC, LRMR, also known as sparse and low-rank matrix decomposition, robust principle component analysis (RPCA) and rank-sparsity incoherence in different applications assumes a large data matrix M decomposed as a sum of low rank matrix L_0 and sparse noise/error matrix S_0. It aims to recover L_0 from corrupted data M. In some applications, however, some of the entries in M may be missing so LRMC problem can be solved as a particular case of LRMR problem [34]. Unlike classical principle component analysis (PCA) applications, the novelty is to make use of error matrix S_0 solely and together with L_0 for image reconstructions. This significantly improves the capability of target detection and the noise susceptibility analysis shows a strong anti-noise ability.

In conclusion, the main contributions of the work presented in this paper are as follows:

- A fast image reconstruction algorithm has been proposed for multipass synthetic aperture THz imaging of multistatic MIMO scenarios. It achieves a high time efficiency because of using 2D FFT and removing stolt interpolations in traditional wavenumber domain algorithms for 3D SAR imaging. Also, it uses zero paddings to compensate the missing data in large sampling scheme and multipass synthetic aperture focusing technique to improve image quality, providing a potential solution to reducing hardware complexity and cost of THz imaging systems.
- A simple sparse imaging scheme with a linear sparse aperiodic array has been verified, providing a practical and cost-effective solution to large aperture imaging applications. The PCPADM algorithm based on LRMR technique is integrated with the aforementioned image reconstruction algorithm for multistatic MIMO sparse imaging. Its novel use of error matrix from LRMR data recovery in image reconstruction and target identification provides additional capabilities for imaging systems.

The rest of this paper is organized as follows. Section II presents the fundamental theory including the low rank matrix recovery for sparse imaging, monostatic approximation for multistatic scenario, zero padding preparing for FFT metheod compatible data and proposed multipass interferometric FFT matched filtering image reconstruction algorithm with/without sparse imaging. Section III provides the experimental setup, measured data and results. Section IV demonstrates wideband imaging for 3D target reconstruction with the simulated data and proposed 2D FFT matched filtering approach. Section V presents the concluding remarks.

II. Fundamental Theory

As illustrated in Fig. 1, a 2D scanning to sample the echo data can be achieved by either a raster scanning with one transceiver or a fully electronic scanning planar array of transceivers [15]. In order to save scanning time in the former scheme or system cost in the latter scheme, a linear sparse aperiodic array is used to achieve the electronic scanning along the horizontal direction and the process is repeated when the array moves Ny times along the vertical direction. Therefore, sparse imaging with a random sampling pattern illustrated in white in Fig.1 will be achieved. Multipass such as N-path phase correlated datasets can be recorded to improve the image quality without increasing the system hardware complexity [37]. In this imaging scheme multiple scans of a target aperture with a path step ds along the horizontal direction are conducted as illustrate in Fig. 1.

This article has been accepted for publication in a future issue of this journal, but has not been fully edited. Content may change prior to final publication. Citation information: DOI10.1109/TMTTXXXXXXXX, IEEE TRANSACTIONS ON MICROWAVE THEORY AND TECHNOLOGIES, VOL. XX, NO. XX, XXXX 2022

The sparse aperiodic array is simply designed from a corresponding linear SPA consisting of full Nt Tx elements and Nr Rx elements. The SPA is a properly designed multistatic MIMO array ($dr = dt \cdot Nt/2$ when Tx elements are located at two ends where dt and dr are Tx and Rx element spacing), so the side lobes of its effective point spread function are minimised [38]. Tx array and Rx array are separated in two lines when necessary [39] as shown in Fig. 2(a). Aperiodic array and sampling pattern can be obtained with few elements in SPA removed. For example, an aperiodic array consisting of 7 Tx and 7 Rx elements are shown in Fig. 1. Consequently, a FFT-based image reconstruction algorithm for sparse imaging is desired.

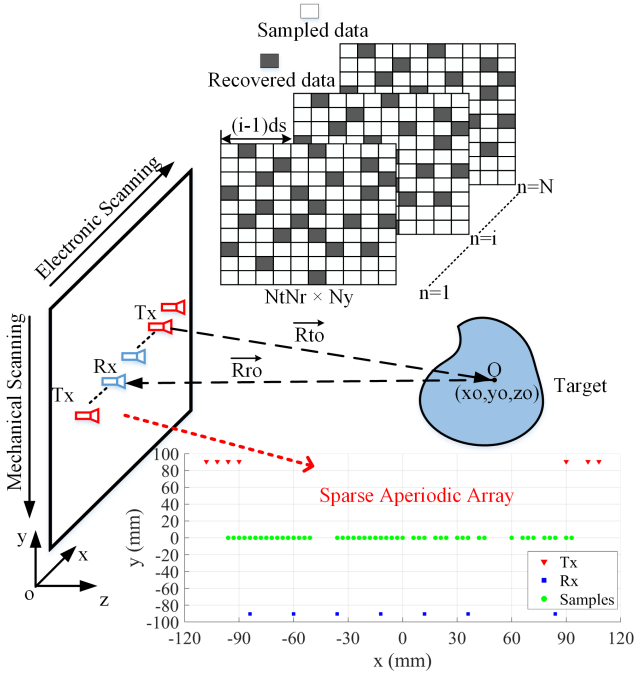

Fig. 1. Proposed multipass interferometric sparse imaging (n indicates nth path sampling aperture and N is the total number of paths).

A. Low Rank Matrix Recovery

According to robust principal component analysis theory, a low-rank matrix data L_0 can be recovered from highly corrupted measurements $M = L_0 + S_0$. Unlike the small noise term N_0 in classical PCA ($M = L_0 + N_0$), the entries in error matrix S_0 can have arbitrarily large magnitude, and their support is assumed to be sparse but unknown [34]. Inspired by this theory, a novel sparse imaging approach using robust principal components analysis is proposed with a particular use of error matrix in target image reconstruction. The nth pass echo data from the target are sampled at $NtNr \times Ny$ scanning positions leading to $S^n_{full} = S^n_{NtNr \times Ny}$ thereafter abbreviated as S_{full} for brevity. It can be either fully measured or recovered/approximated as $\hat{S}_{full}$ from its few observations S_{obs} - random sampled data - by the proposed sparse imaging technique,

$$S_{obs}(i,j) = P_{\Omega_{obs}} \cdot S_{full} = \begin{cases} S_{full}(i,j), & (i,j) \in \Omega_{obs} \\ 0, & (i,j) \notin \Omega_{obs} \end{cases} \quad (1)$$

where $P_{\Omega_{obs}}$ is a random matrix consisting of 0 (black) and 1 (white) to deploy the random sampling and Ω_{obs} indicates a space of samples measured. Only active samples and associated channels will be implemented in a practical system. According to related theory [32], [40], the missing echo data can be completed by solving the following nuclear norm minimization optimization problem,

$$\begin{aligned} \text{minimize} \quad & \|L_{full}\|_* + \lambda_s \|S_{error}\|_1 \\ \text{subject to} \quad & P_{\Omega_{obs}} \cdot (L_{full} + S_{error}) = S_{obs} \end{aligned} \quad (2)$$

where λ_s is a scalar. $\|L_{full}\|_*$ is the nuclear norm of component matrix $L_{full} \in C^{(N_t N_r) \times N_y}$ abbreviated as L matrix below for brevity, which is the sum of its singular values [40], and $\|S_{error}\|_1$ refers to the l_1-norm of sparse error matrix. Principal component pursuit by alternating directions is used to solve (2) [34]. Unlike the classical PCA to recover L matrix data from measurements, the recovered $\hat{S}_{full}$ for sparse imaging can be L_{full}, S_{error} or their sum $L_{full} + S_{error}$.

B. Monostatic Approximation and Central Zero Padding

Since we are dealing with a multistatic imaging scenario, the separation between transmitter and receiver is too large to be approximated with their center when calculating the round-trip phase. It is impossible to apply FFT-based image reconstruction technique directly, generalized synthetic aperture focusing technique was thereby used [37], [39]. Thus, we first use an effective monostatic approximation for the captured raw data [16], [18]. By using this approximation, the received data phase of each Tx-Rx interaction is modified according to the position of the physical antennas and the corresponding virtual element [20]. Suppose $(x, y, 0)$ is the position of phase center corresponding to the transmitter element at $(x_t, y_t, 0)$ and the receiver element at $(x_r, y_r, 0)$. The multistatic data set can be converted to an effective monostatic form by

$$\tilde{s}_{x,y} = s(x_t, y_t, x_r, y_r) \frac{s_o(x,y)}{s_o(x_t, y_t, x_r, y_r)} \quad (3)$$

where $s(x_t, y_t, x_r, y_r)$ is the entry of fully measured S_{full} or recovered $\hat{S}_{full}$ if LRMR is used, $s_o(x,y)$ and $s_o(x_t, y_t, x_r, y_r)$ correspond to the monostatic and multistatic reference signals, respectively. The above conversion provides a mathematical approximation of an equivalent monostatic topology. The converted data is referred to as as $\tilde{S}(x,y) \in C^{(N_t N_r) \times N_y}$.

As shown in Fig. 2(a), due to one gap in the center of the equivalent virtual (monostatic) sampling data when using a linear SPA, the converted data $\tilde{S}$ is not yet readily compatible with Fourier-based image reconstruction technique. This is padded with zero in this paper. The consequent data is called $\bar{S}(x,y) \in C^{(N_t N_r + 1) \times N_y}$.

C. Internal Zero Padding and Proposed Multipass FFTMF Imaging Algorithm

Aforementioned monostatic approximation and central zero padding comply with the standard FFT matched filtering approach [21], [41]. The data spacing in $\bar{S}$ might be much larger than the $\lambda/2$ required by Nyquist sampling criterion,

This article has been accepted for publication in a future issue of this journal, but has not been fully edited. Content may change prior to final publication. Citation information: DOI10.1109/TMTTXXXXXXXX

which are dv at y-mechanical scanning direction and $dt/2$ at x-electronic scanning direction under the scheme. It is found from our study that a finer discretization is helpful to improve the target image quality, we therefore propose the internal zero padding on $\bar{S}$ to achieve a denser echo data so resulting in a finer target image discretization. The padding along the electronic scanning direction is illustrated in Fig. 2(b) where only half data of left part is shown for brevity.The consequent data is referred to as $\bar{S}'(x,y)$.

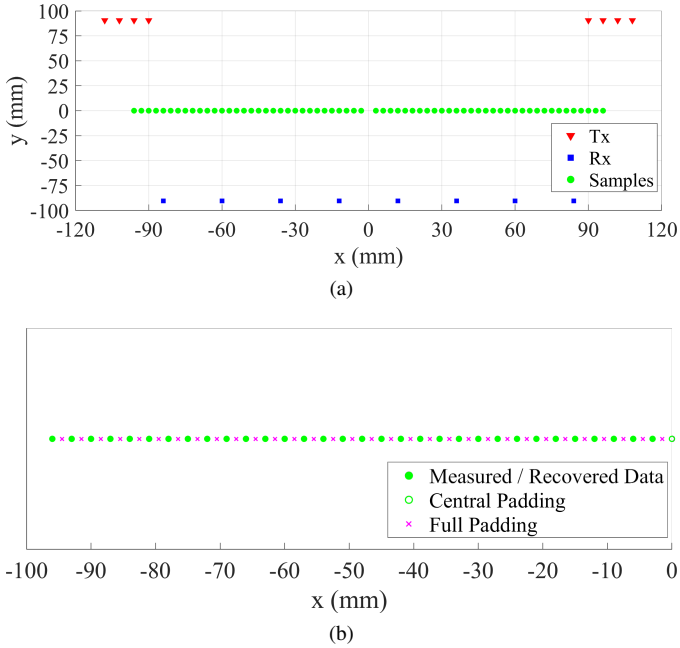

Fig. 2. (a) Positions of SPA and its initial virtual samples (b) samples zoomed in on the left half of (a) and zero padding.

On the basis of FFT matched filtering and multipass interferometric synthetic aperture imaging, a 2D target reflectivity function $G(x,y,z_0)$ at a fixed distance z_0 can be reconstructed by

$$G(x,y,z_0)=\sum_{n=1}^{N}\left\langle FT_{2D}^{-1}\left\{FT_{2D}\left[\bar{S}'\right]FT_{2D}\left[H_{z_0}^{*}\right]\right\}\right\rangle \quad (4)$$

where $H_{z_0}^{*}$ is the matrix of $h_{z_0}^{*}(x,y)=e^{j2k\sqrt{(x-n\cdot ds)^2+y^2+z_0^2}}$ that is the conjugate of system response evaluated at the focusing point (x,y,z_0). FT_{2D} and FT_{2D}^{-1} are 2D fast Fourier transform and inverse fast Fourier transform, respectively. Unlike the tradiational FFT mached filtering, newly introduced $n\cdot ds$ depicts the improved multipass FFTMF with an interferometric imaging technique. When wideband imaging is used, a 3D target reflectivity function $G(x,y,z)$ can be reconstructed by

$$G(x,y,z)=\sum_{nf=1}^{Nf}\sum_{n=1}^{N}\left\langle FT_{2D}^{-1}\left\{FT_{2D}\left[\bar{S}'\right]FT_{2D}\left[H_{z,nf}^{*}\right]\right\}\right\rangle \quad (5)$$

where the entry of matrix $H_{z,nf}^{*}$ is $h_{nf}^{*}(x,y,z)=e^{j2k_{nf}\sqrt{(x-n\cdot ds)^2+y^2+z^2}}$ that is the conjugate of system response of k_{nf} wave at the focusing point (x,y,z). The internal padding is not used when $\bar{S}'(x,y)$ is replaced by $\bar{S}(x,y)$. In addition, it implies sparse imaging used if $\bar{S}'(x,y)$ or $\bar{S}(x,y)$ are derived from the recovered $\hat{S}_{full}$ rather than the exact measured S_{full}. The proposed 3D image reconstruction of (5) is simplified to a 2D Fourier transform only and it is time-efficient because it does not require a stolt interpolation in spatial frequency domain [23], [24]. Thus we conclude the proposed multipass interferometric FFTMT image reconstruction algorithm with PCPADM for multistatic MIMO sparse imaging in Table I [34].

TABLE I
PROPOSED FFTMF ALGORITHM FOR MULTISTATIC MIMO INTERFEROMETRIC SYNTHETIC APERTURE IMAGING

Input: Sparse sampling matrix P, measured matrix data $S_{full}\in C^{(N_tN_r)\times N_y}$ or its sparse samples S_{obs}, scalar λ_s, tolerance ϵ, threshold μ , maximum iteration count k_{max} [34]

Output: 2D reconstruction $G(x,y,z_0)$ or 3D reconstruction $G(x,y,z)$

1. If sparse imaging is not used, $\hat{S}_{full}=S_{full}$ and go to step 6, else start from step 2
2. Set $S_0=Y_0=0,\mu>0,M=S_{obs}$
3. for $k=1$ to k_{max}
   while not converge do
   if $k>1$ & $\|P\cdot(M-L_{k+1}-S_{k+1})\|_F/\|M\|_F\le\epsilon$ then break
   Compute $L_{k+1}=D_{1/\mu}(M-S_k+\mu^{-1}Y_k)$
   Compute $S_{k+1}=S_{\lambda_s/\mu}(M-L_{k+1}+\mu^{-1}Y_k)$
   Compute $Y_{k+1}=Y_k+\mu P\cdot(M-L_{k+1}-S_{k+1})$
   end while
4. end
5. Set $\hat{S}_{full}=L^{k+1},S^{k+1}$ or $L^{k+1}+S^{k+1}$
6. Apply monostatic approximation on $\hat{S}_{full}$ with (3) to get $\tilde{S}_{NtNr\times Ny}$
7. Get $\bar{S}_{NtNr\times(Ny+1)}$ by using central zero padding
8. Get $\bar{S}'$ by using internal zero padding
9. Reconstruct image with (4) or (5) for 2D or 3D reconstructions, respectively

For a matrix X, S_τ denotes the shrinkage operator
$S_\tau(X)=sgn(X)\cdot max(|X|-\tau,0)$
$D_\tau(X)$ denotes the singular value thresholding operator
$[U,\Sigma,V]=SVD(X)$
$D_\tau(X)=US_\tau(\Sigma)V^*$

* sgn and max indicate the sign function and maxima function, SVD represents singular value decomposition, Σ is a diagonal matrix with singular values $\sigma_1,\sigma_2,\sigma_3,\cdots$

D. Metrics of Image Quality

Image entropy (IE) and image contrast (IC) are adopted to quantitatively evaluate the image quality. Entropy can be used to measure the smoothness of a distribution function. The smoother a distribution function is, the larger the entropy is. This usually includes rich details. A sharper image results in a smaller entropy [42]. IC represents the color richness of the image. And high IC indicates a high difference in brightness between light and dark areas of an image.

$$IE=-\sum_{i=1}^{m}\sum_{j=1}^{n}\frac{|g_{i,j}|^2}{\|G\|_F^2}\ln\frac{|g_{i,j}|^2}{\|G\|_F^2} \quad (6)$$

$$IC=\sqrt{\frac{mn}{\|G\|_F^4}\sum_{i=1}^{m}\sum_{j=1}^{n}|g_{i,j}|^4-1} \quad (7)$$

where $g_{i,j}$ and $\|G\|_F$ are the entry and Frobenius norm of target image matrix G.

III. Experiment and Measured Results

A schematic of the experimental imaging system in the lab is shown in Fig. 3. A Keysight PNA-X-N5244A is connected to OML WR-03 extension modules for transmitting and receiving the THz signal. They move to each position of Tx and Rx elements so as to imitate the Tx and Rx sub-arrays in a SPA, respectively. Since the linear scanning stages are fixed, the target is mounted on a NSI-MI planar near field measurement system of PNF-XYV-0.9 m $\times$ 0.9 m, moving vertically to inversely imitate a relatively mechanical scanning of the SPA to a fixed target. The photographs of whole imaging system and linear scanning stages are shown in Fig. 4(a) and Fig. 4(b) in which the Tx sub-array and Rx sub-array is separated by 181 mm along the vertical direction in the experiments because of the size of WR-03 extension modules. A pure metallic target and a dielectric target with metallic patterns under test are shown in Fig. 4(c) and 4(d). The experimental setup is summarized in Table II. The target distances of both kinds of experiments are 1.4 m. Two array elements of horns utilized in the experiment are WR3 (220 $\sim$ 325 GHz) standard pyramidal horns with a peak gain of about 23.81 dB at 220 GHz and the typical output power from the THz frequency extension head at 220 GHz is -13 dBm (0.05 mW) [39]. We noted that increasing the dt value in a SPA will increase the array aperture size, thus, theoretically, a superior spatial resolution can be obtained. However, it will also cause artifacts in the image. Also, we found that the spatial space period of ghost images is also related to the spacing dt and target distance [39]. In order to meet desired imaging demands, the synthesized full SPA consists of $Nt = 8$ and $Nr = 8$ elements, Tx element spacing dt is 6 mm so the electronic sampling spacing is 3 mm and the real aperture length is 216 mm. The mechanical scanning length of imaging the metallic target is 0.3 m with a step of 4 mm. The pass step ds is 20 mm and 4-pass datasets are collected. The mechanical scanning length of imaging the dielectric target is 0.4 m with a step of 2.5 mm. The pass step ds is 10 mm and 5-pass datasets are collected. Accordingly, the single-pass sparsity rates are 3.87% and 4.65% while the multipass sparsity rates are 15.50% and 23.24%. Single-pass sparsity rate (SSR) is defined as the ratio of single-pass sampling data with the full SPA to Nyquist half a wavelength sampling data. Multipass sparsity rate (MSR) is equal to the SSR multiplied by the number of passes. It is shown that even though the random sparse imaging with a aperiodic array is further used, the proposed SPA imaging scheme has already reduced the sampling data significantly.

A. Effect of Zero Padding

There are 10 holes within the pure metallic target (145 mm $\times$ 120 mm $\times$ 5 mm) ranging from 5 to 7 mm in diameter. The reconstructed 4-pass interferometric synthetic aperture focusing images are compared in Fig. 5. Fig. 5(a) shows the reconstructed image with central padding of zeros only so the data spacing along x and y-axis are 3 mm and 4 mm. Fig. 5(b) shows the reconstructed image with central padding and internal padding of zeros so achieving 0.75 mm and 1 mm data spacing along x and y-axis. Fig. 5(c) shows the sparse imaging output with an aperiodic array of 7 Tx & 7 Rx elements (49 sampling points along x-axis). Fig. 5(d) shows the image reconstructed by 4-pass interferometry GSAFT without any data padding as a reference. Comparing Fig. 5(a) to Fig. 5(b), it is seen that the contours of holes are improved after using both central and internal padding of zeros because of denser image pixels. This agrees with a higher IE improving from 7.288 to 10.060 and the image contrast stays stable of 1.48 as summarized in Table III. The sparse imaging output shown in Fig. 5(c) with the reconstruction approach of PCPADM-FFTMF and zero padding has achieved the aim of reducing the number of transceivers/sampling data without compromising on image quality verified as little decreases in IE and IC in comparison with Fig. 5(b). Thus, the proposed FFT matched filtering reconstruction approach shows comparable image quality in comparison with the reference of Fig. 5(d) reconstructed by a GSAFT approach.

TABLE II
Experimental Setup Parameters: Target Distance 1.4 m

Target (Size / mm $\times$ mm $\times$ mm)	Mechanical Spacing (Length)	Pass Step ds (Number)	SSR (MSR)
Metal-Fig.4(c)	4.0 mm	20 mm	3.87%
(145 $\times$ 120 $\times$ 5)	(0.3 m)	(4)	15.50%
Dielectric-Fig.4(d)	2.5 mm	10 mm	4.65%
(260 $\times$ 180 $\times$ 1.6)	(0.4 m)	(5)	23.24%

TABLE III
IE and IC of Metallic Target Images in Fig. 5

Metrics	Fig.5(a)	Fig.5(b)	Fig.5(c)	Fig.5(d)
Image Pixels	52 $\times$ 150	208 $\times$ 328	208 $\times$ 328	208 $\times$ 328
Image Entropy	7.288	10.060	10.059	10.120
Image Contrast	1.481	1.480	1.477	1.428

B. Investigation on Sparse Data Recovery with PCPADM

In addition, the target of metallic patches etched on the dielectric substrate (260 mm $\times$ 180 mm $\times$ 1.6 mm) as shown Fig. 4(d), which is more challenging because the contrast between metal to dielectric is smaller, has been tested. The reconstructions of using L matrix and S_{error} matrix solely

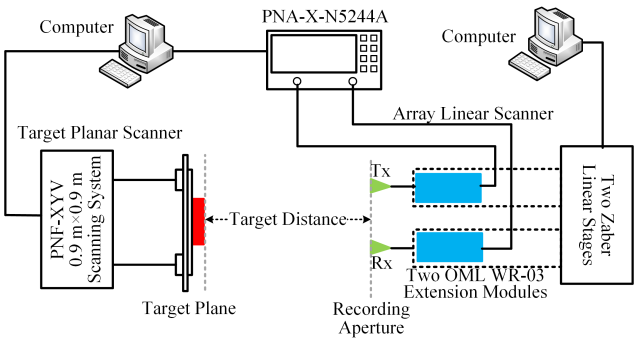

Fig. 3. Schematic of the experimental imaging system in the lab.

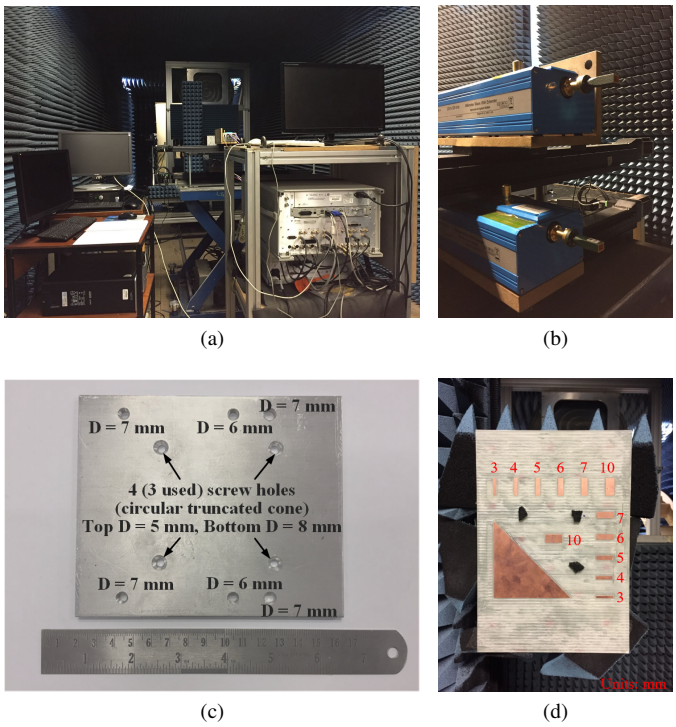

Fig. 4. Photographs of experimental (a) whole imaging system (b) MIMO linear scanning stages (c) pure metallic target (d) dielectric target with metallic pattern [17].

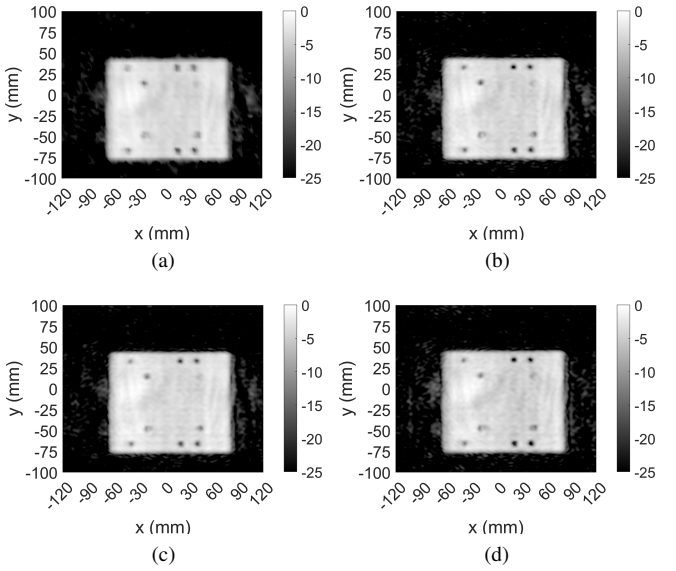

Fig. 5. Reconstructed 4-pass interferometric synthetic aperture focusing images (units: dB) of metallic target with FFT matched filtering (a) central padding of zeros (b) central padding and internal padding of zeros (c) same padding as (b) but with sparse imaging of an aperiodic array of 7 Tx & 7 Rx elements (d) with interferometry GSAFT as reference (no zero padding).

have been investigated in Fig. 6. Fig. 6(a) and 6(b) show the reconstructed images with L matrix and S_{error} matrix solely in which an aperiodic array of 6 Tx and 6 Rx elements is used, respectively. The reconstructions of using L matrix reveal a full view of the target and a light shadowing of metallic patterns. This shows a lower IC of 1.440 and a higher IE of 11.069 because different properties of targets are included, as summarized in Table IV. In contrast, the reconstructions

TABLE IV
IE AND IC OF CHALLENGING DIELECTRIC TARGET IMAGES WITH SAME IMAGE PIXELS OF 390 × 408

Metrics	Fig.6(a)	Fig.6(b)	Fig.7(a)	Fig.6(c)	Fig.6(d)	Fig.7(b)
IE	11.069	10.924	11.062	11.049	10.798	11.025
IC	1.440	2.039	1.500	1.477	2.338	1.558
Metrics	Fig.7(c)	Fig.7(d)	Fig.8(a)	Fig.8(b)	Fig.8(c)	Fig.8(d)
IE	11.007	11.039	11.066	11.103	11.150	11.329
IC	1.588	1.570	1.544	1.829	1.504	1.442

of using S_{error} matrix suppress the view of substrate layer and consequently the view of metallic patterns is enhanced. This agrees with an increasing IC of 2.039 and a lower IE of 10.924. Both kinds of reconstructions are complementary to each other. Same trends are found in Fig. 6(c) and 6(d) reconstructed with L matrix and S_{error} matrix solely in which an aperiodic array of 7 Tx and 7 Rx elements is used. Besides, an improved image quality is obtained because more data are sampled for the image reconstruction.

In order to incorporate both advantages, reconstructions with $\hat{S}_{full} = L_{full} + S_{error}$ are compared in Fig. 7(a) and Fig. 7(b) in which aperiodic arrays of 6 Tx & 6 Rx elements and 7 Tx & 7 Rx elements are used. Compared with Fig. 6(a) and Fig. 6(c), the ICs increase in Fig. 7(a) and Fig. 7(b) so the targets become clear and they are more likely to be recognised. Meanwhile, details become more visible in comparison with Fig. 6(b) and Fig. 6(d), which is verified by higher IEs. In addition, the reconstructions of using a full sampling with the proposed FFTMF approach and GSAFT as a reference are shown in Fig. 7(c) and Fig. 7(d). Compared with the most accurate reconstruction based on GSAFT, the proposed FFTMF reconstruction approach with full sampling data offers similar image quality with IC increasing from 1.570 to 1.588 and IE decreasing from 11.039 to 11.007, which agrees with the visual evaluation that no visible differences can be found. Moreover, the proposed FFTMF sparse imaging is capable of proving equivalent image quality as the FFTMF full imaging in both the visible evaluation and quantitative evaluations of IE and IC. In summary, the full matrix reconstruction is proposed for imaging differentiating from classical PCA applications. Besides, the reconstruction of using S_{error} matrix is helpful to identify the metallic pattern. Thus, it is proposed to be a complementary reconstruction/detection in addition to the full matrix reconstruction.

C. Analysis on Noise Susceptibility

It is known that error matrix in PCA correlates with noise. Therefore, the noise susceptibility of the proposed imaging approach has been investigated on basis of Fig. 7(b). The white Gaussian noise is added on the measured (sparse) data to achieve 9 dB and 3 dB signal-to-noise ratios, respectively. It is worth differentiating this additional noise from the experimental noise which has already been included in the measured data. The reconstructions of a sum matrix and a error matrix with 9 dB SNR are shown in Fig. 8(a) and 8(b). In comparison, Fig. 8(c) and 8(d) show the reconstructions of a sum matrix and a error matrix with 3 dB SNR. Comparing Fig. 8(a) and

This article has been accepted for publication in a future issue of this journal, but has not been fully edited. Content may change prior to final publication.
Citation information: DOI10.1109/TMTTXXXXXXXX, IEEE TRANSACTIONS ON MICROWAVE THEORY AND TECHNOLOGIES, VOL. XX, NO. XX, XXXX 2022

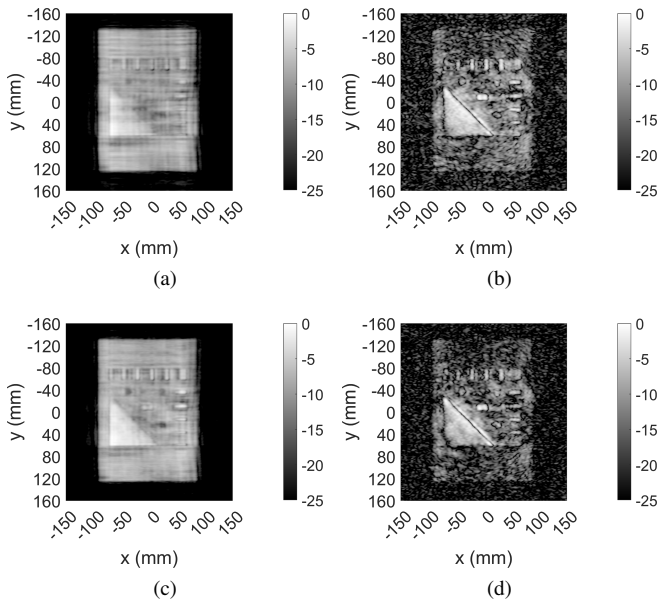

Fig. 6. Reconstructed 5-pass interferometric synthetic aperture focusing images (units: dB) of the dielectric target with the proposed FFTMF approach and sparse sampling data. Aperiodic array of 6 Tx & 6 Rx elements and reconstructions of (a) L matrix only or (b) S_{error} matrix only, aperiodic array of 7 Tx & 7 Rx elements and reconstructions of (c) L matrix only or (d) S_{error} matrix only.

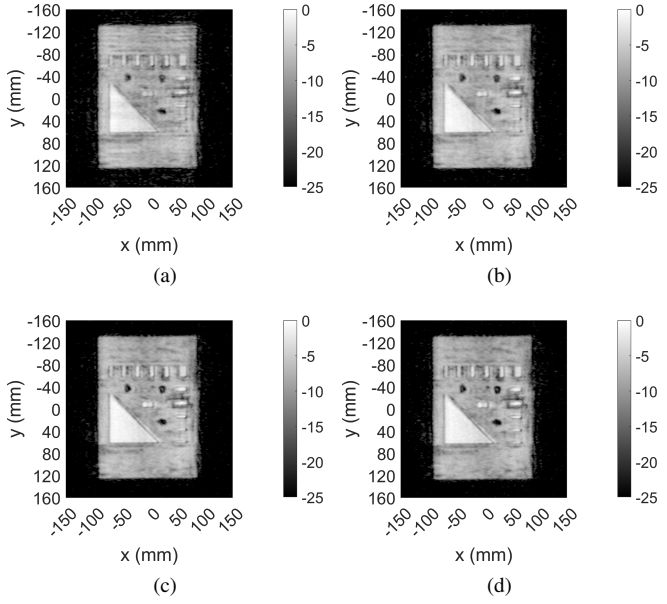

Fig. 7. Reconstructed 5-pass interferometric synthetic aperture focusing images (units: dB) of the dielectric target using the proposed FFTMF approach and an aperiodic array of (a) 6 Tx & 6 Rx elements (b) 7 Tx & 7 Rx elements (c) a full SPA of 8 Tx& 8 Rx elements and (d) reference of using mutlipass interferometric GSAFT with the full SPA sampling data.

8(c) with Fig. 7(b), we can see the deterioration of image quality with the decease of SNR but the impact is very small, which is further verified by little decrease in IC from 1.558 to 1.544 and 1.504. Therefore, it is still feasible to achieve the imaging and target detection successfully even when SNR is reduced as low as 3 dB. Regarding the reconstruction of using an error matrix only, compared Fig. 8(b) with Fig. 8(a), an improved image contrast is obtained and the metallic pattern can be recognised more clear, as revealed before. When the SNR decreases to 3 dB, although the recognition of metallic pattern is still clear, the image contrast drops because of too much noise in the surroundings/background. Therefore, the proposed imaging/detection approach making use of this error matrix shows a strong anti-noise ability.

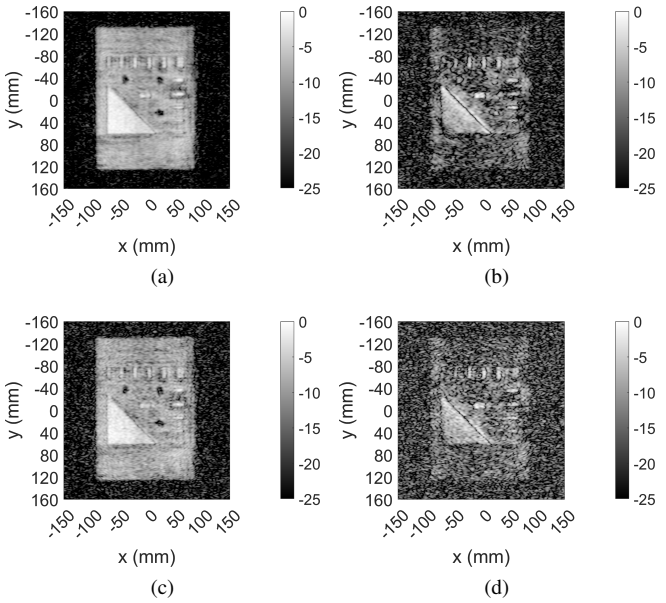

Fig. 8. Reconstructed 5-pass interferometric synthetic aperture focusing images (units: dB) of Fig. 7(b) with 9 dB SNR and reconstruction of (a) full matrix (b) S_{error} matrix and with 3 dB SNR and reconstruction of (c) full matrix (d) S_{error} matrix.

D. Tolerance to Target Focusing Distance

THz imaging is thought to be sensitive to focusing distance because a small distance error will incur significant phase errors with respect to such a short wavelength. Therefore, the reconstructed images with the proposed sparse imaging (same configuration as Fig. 7(b)) with a range of target distances from 1.38 m to 1.50 m are compared in Fig. 9. In comparison, the reconstructed images with the GSAFT approach (same configuration as Fig. 7(d)) at different focusing distances are shown in Fig. 10. The proposed sparse imaging approach demonstrates equivalent capacity as the most accurate GSAFT approach. In addition, the measured distances in the experiments from the target to input plan and output plane of horn antennas are 1.47 m and 1.40 m, respectively. It is reasonable to find a little improvement on contour of metallic patches in the center and right bottom areas of Fig. 9(c) and Fig. 9(d) when focusing target distances are 1.46 m and 1.50 m. However, such tiny differences are seen in reconstructions within such a wide distance range, which shows an unexpected stability of successful target detection to target focusing distance error.

E. Comparison of Image Reconstruction Time

Another key metric for imaging/detection is imaging frame rate which is desired to be as fast as possible, up to few seconds per frame for real time detection. Therefore, the statistic

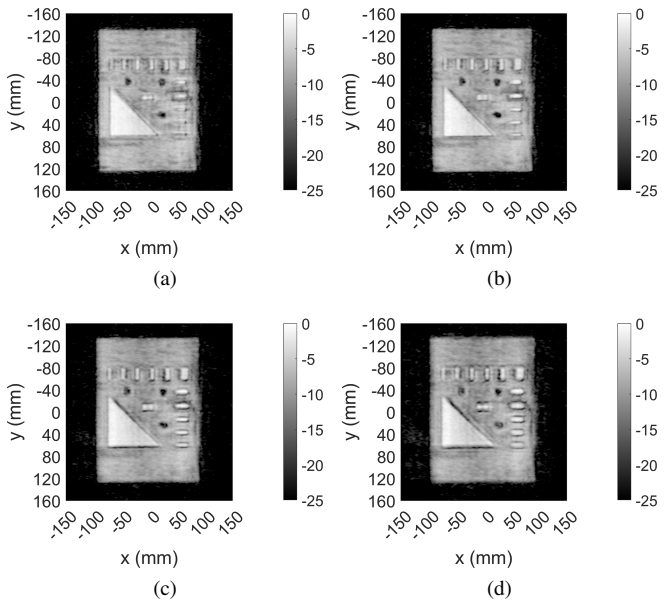

Fig. 9. Reconstructed 5-pass interferometric synthetic aperture focusing images (units: dB, same configurations as Fig. 7(b)) with the proposed sparse imaging at a varying target distance of (a) 1.38 m (b) 1.42 m (c) 1.46 m (d) 1.50 m.

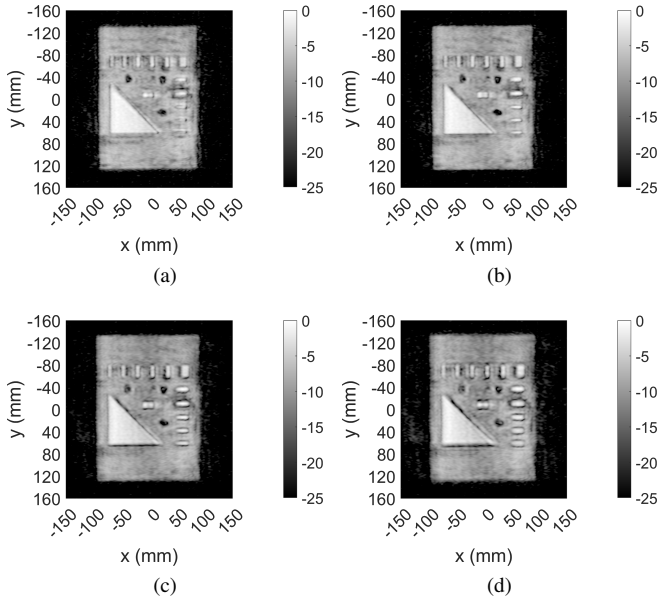

Fig. 10. Reconstructed 5-pass interferometric synthetic aperture focusing images (units: dB, same configurations as Fig. 7(d)) with full sampling and GSAFT approach at a varying target distance of (a) 1.38 m (b) 1.42 m (c) 1.46 m (d) 1.50 m.

image reconstruction time with 30 independent attempts of dielectric target in different schemes has been investigated as shown in Fig. 11 and Table V. The platform under test is MATLAB on a desktop with windows 10 Enterprise, Intel Core I7-10700 and random access memory of 16 GB. The FOV is 192 mm $\times$ 400 mm and the target reconstruction area is 300 mm $\times$ 320 mm. GSAFT-A_1 and A_2 represent the images are reconstructed by multipass interferometric GSAFT [17] but the image is discretized into 4 mm and 2 mm grids, respectively. The latter image computation is fourfold so the reconstruction time increases to 15.72 s from 3.72 s. Therefore, it is approximated about 1.5 minutes if the pixel size is reduced to 0.75 mm $\times$ 0.83 mm. However, the time reduces significantly when the proposed FFTMF is used. The full sampling data of 8 Tx and 8 Rx elements are used in FFTMF-B_1 and FFTMF-B_2 so there is no compromise on image quality. Moreover, the zero padding is used to achieve 1.50 mm $\times$ 1.25 mm and 0.75 mm $\times$ 0.83 mm image pixels, respectively. The corresponding image reconstruction time are 0.23 s and 0.25 s, respectively, although both image discretizations are much denser than GSAFT-A_2, the achieved reconstruction speed is promising for real time detection. In addition, the tiny difference of reconstruction time indicates that the FFTMF approach is not so sensitive to the target data volume like GSAFT method. Even though the proposed sparse imaging technique of 60%, 70% and 80% sampling data are used, the image quality reconstructed with full matrix will not constrain the target identification as demonstrated in our previous LRMC sparse imaging while newly proposed reconstructions with the error matrix provides additional identification ability [17]. The image reconstruction time increases to the range of 2.0-3.0 s with a threshold $u_1 = 20\lambda_s$ because of full data recovery in each pass, as shown in FFTMF-B_3 to B_5. It is worth noting that lower u will increase the reconstruction time as shown in FFTMF-B_6 to B_8 with $u_2 = 10\lambda_s$, which ranges from 2.97 s to 4.16 s for a 5-pass synthetic aperture focusing image reconstruction.

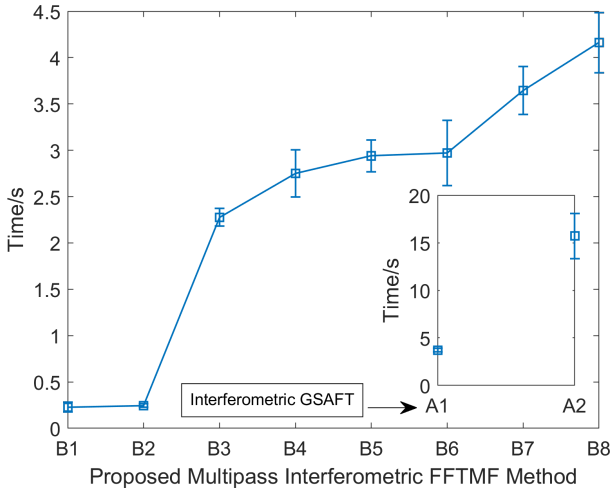

Fig. 11. Image (5 passes in total) reconstruction time with 30 times in each scheme, the top and bottom lines in each scheme imply the deviation in 30 reconstructions.

IV. Wideband Imaging for 3D Target Reconstruction

In order to verify the 3D target reconstruction, a simulation of wideband imaging on a T-shaped target is conducted. The full SPA is same as the experimental configuration used. The target distance is 1.1 m. The mechanical scanning length is 200 mm with a step of 2 mm. The bandwidth is 15 GHz with a center frequency of 220 GHz and the number of frequency

TABLE V
COMPARISON OF IMAGE RECONSTRUCTION TIME IN FIG. 11

Scheme	Sparse Imaging	Image Pixel Size(x&y)	Mean/Second
GSAFT-A_1	NA	4.00 mm & 4.00 mm	3.72
GSAFT-A_2	NA	2.00 mm & 2.00 mm	15.72
FFTMF-B_1	NA	1.50 mm & 1.25 mm	0.23
FFTMF-B_2	NA	0.75 mm & 0.83 mm	0.25
FFTMF-B_3	60%/μ_1	0.75 mm & 0.83 mm	2.28
FFTMF-B_4	70%/μ_1	0.75 mm & 0.83 mm	2.75
FFTMF-B_5	80%/μ_1	0.75 mm & 0.83 mm	2.94
FFTMF-B_6	60%/μ_2	0.75 mm & 0.83 mm	2.97
FFTMF-B_7	70%/μ_2	0.75 mm & 0.83 mm	3.65
FFTMF-B_8	80%/μ_2	0.75 mm & 0.83 mm	4.16

* The percentages in sparse imaging column indicate the proportion of S_{obs}/S_{full} in 1

samples are 220. Such a bandwidth is capable of providing a 10 mm range resolution at 1.1 m. The T-shaped target in simulation consists of 100×100 pixels with a grid distance of 1 mm. The reconstructed images of SPA full imaging and aperiodic array sparse imaging are shown in Fig. 12(a) and Fig. 12(b). It is shown that 3D target images are both reconstructed successfully. It is worth mentioning that the effective sampling spacing of non-zero samples (data) along x-axis and y-axis are 3 mm and 2 mm, respectively. That is much larger than the $\lambda/2$ and even λ. The thickness of 10 mm reveals the range resolution. There is little deterioration on the surface of target in sparse imaging but it is acceptable when taking account of the large sampling spacing used and it does not hinder the target recognition.

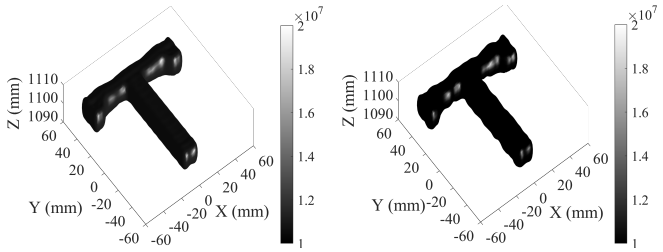

Fig. 12. Reconstructed 3D images (units: linear) of T-shaped target (a) SPA full sampling and imaging and (b) sparse imaging of aepridoc arrays with 7 Tx & 7 Rx elements.

V. CONCLUSION

A novel FFT matched filtering reconstruction algorithm has been proposed for THz multipass synthetic aperture imaging with a multistatic MIMO configuration. The SPA already saves sampling data ratio to 5% below in a single-pass imaging and 25% below in a multipass imaging in the experiments. The sparse sampling scheme is cost effective and feasible to implement in practice with a simple design of aperiodic array originating from the SPA. In addition, the proposed sparse imaging with the use of a aperiodic array and a robust principal component analysis algorithm is not only promising for further saving the number of transceivers or size of the sampling data, but also contributes to improving the target detection by using the error matrix in image reconstruction. We showed that the proposed imaging approach is capable of reconstructing one 5-pass synthetic aperture image in about 0.25 s for an imaging area of 192 mm $\times$ 400 mm when sparse imaging approach is not used and in about 2.0-4.0 s when sparse imaging approach is used. Finally, a strong anti-noise ability, a high tolerance to target focusing distance and a successful 3D target imaging were demonstrated.

REFERENCES

[1] S. S. Ahmed, "Microwave imaging in security—two decades of innovation," *IEEE J. Microwaves*, vol. 1, no. 1, pp. 191–201, Jan. 2021.
[2] N. A. Salmon, "Indoor full-body security screening: Radiometric microwave imaging phenomenology and polarimetric scene simulation," *IEEE Access*, vol. 8, pp. 144 621–144 637, Aug. 2020.
[3] B. Wang, S. Zhong, T.-L. Lee, K. S. Fancey, and J. Mi, "Non-destructive testing and evaluation of composite materials/structures: A state-of-the-art review," *Advances in Mechanical Engineering*, vol. 12, no. 4, pp. 1–28, Apr. 2020.
[4] M. Nezadal, J. Schür, and L.-P. Schmidt, "Non-destructive testing of glass fibre reinforced plastics with a synthetic aperture radar in the lower thz region," in *2012 37th International Conference on Infrared, Millimeter, and Terahertz Waves*, Sep. 2012, pp. 1–2.
[5] I. Amenabar, F. Lopez, and A. Mendikute, "In introductory review to thz non-destructive testing of composite mater," *J. Infrared Milli. Terahz Waves*, vol. 34, no. 2, pp. 152–169, Feb. 2013.
[6] S. López-Tapia, R. Molina, and N. P. de la Blanca, "Deep cnns for object detection using passive millimeter sensors," *IEEE Trans. Circuits Syst. Video Technol.*, vol. 29, no. 9, pp. 2580–2589, 2019.
[7] Z. Wang, T. Chang, and H.-L. Cui, "Review of active millimeter wave imaging techniques for personnel security screening," *IEEE Access*, vol. 7, pp. 148 336–148 350, 2019.
[8] H. Tu, X. Meng, Z. Sun, L. Chen, C. Fang, Y. Zhu, H. Zhang, J. Zhang, and C. Fang, "A fast 220-ghz real aperture 3-d personnel screening system with a novel-shaped mirror design," *IEEE Trans. Terahertz Sci. Technol.*, vol. 9, no. 3, pp. 253–261, 2019.
[9] D. Damyanov, A. Batra, B. Friederich, T. Kaiser, T. Schultze, and J. C. Balzer, "High-resolution long-range thz imaging for tunable continuous-wave systems," *IEEE Access*, vol. 8, pp. 151 997–152 007, 2020.
[10] A. Zhuravlev, V. Razevig, M. Chizh, G. Dong, and B. Hu, "A new method for obtaining radar images of concealed objects in microwave personnel screening systems," *IEEE Trans. Microw. Theory Techn.*, vol. 69, no. 1, pp. 357–364, 2021.
[11] M. Abbasi, A. Shayei, M. Shabany, and Z. Kavehvash, "Fast fourier-based implementation of synthetic aperture radar algorithm for multi-static imaging system," *IEEE Trans. Instrum. Meas.*, vol. 68, no. 9, pp. 3339–3349, 2019.
[12] M. E. Yanik, D. Wang, and M. Torlak, "Development and demonstration of mimo-sar mmwave imaging testbeds," *IEEE Access*, vol. 8, pp. 126 019–126 038, 2020.
[13] B. Cheng *et al.*, "340-ghz 3-d imaging radar with 4tx-16rx mimo array," *IEEE Trans. Terahertz Sci. Technol.*, vol. 8, no. 5, pp. 509–519, Sep. 2018.
[14] F. Gumbmann and A. Schiessl, "Short-range imaging system with a nonuniform sfcw approach," *IEEE Trans. Microw. Theory Techn.*, vol. 65, no. 4, pp. 1345–1354, Apr. 2017.
[15] S. S. Ahmed, A. Schiessl, and L.-P. Schmidt, "A novel fully electronic active real-time imager based on a planar multistatic sparse array," *IEEE Trans. Microw. Theory Techn.*, vol. 59, no. 12, pp. 3567–3576, Dec. 2011.
[16] Z. Wang, Q. Guo, X. Tian, T. Chang, and H.-L. Cui, "Near-field 3-d millimeter-wave imaging using mimo rma with range compensation," *IEEE Trans. Microw. Theory Techn.*, vol. 67, no. 3, pp. 1157–1166, Mar. 2019.
[17] S. Hu, C. Shu, Y. Alfadhl, and X. Chen, "Advanced thz mimo sparse imaging scheme using multipass synthetic aperture focusing and low-rank matrix completion techniques," *IEEE Trans. Microw. Theory Techn.*, 2021.
[18] W. F. Moulder, J. D. Krieger, J. J. Majewski, C. M. Coldwell, H. T. Nguyen, D. T. Maurais-Galejs, T. L. Anderson, P. Dufilie, and J. S. Herd, "Development of a high-throughput microwave imaging system for concealed weapons detection," in *2016 IEEE International Symposium on Phased Array Systems and Technology (PAST)*, 2016, pp. 1–6.

[19] S. Li, S. Wang, Q. An, G. Zhao, and H. Sun, "Cylindrical mimo array-based near-field microwave imaging," *IEEE Trans. Antennas Propag.*, vol. 69, no. 1, pp. 612–617, 2021.

[20] A. M. Molaei, O. Yurduseven, and V. Fusco, "An efficient waveform diversity based on variational mode decomposition of coded beat-frequency shifted signals algorithm for multiple-input multiple-output millimetre-wave imaging," *IET Radar, Sonar & Navig.*, vol. 15, no. 10, pp. 1266–1280, May 2021.

[21] A. M. Molaei, S. Hu, V. Skouroliakou, V. Fusco, X. Chen, and O. Yurduseven, "Fourier compatible near-field multiple-input multiple-output terahertz imaging with sparse non-uniform apertures," *IEEE Access*, pp. 1–1, Nov. 2021.

[22] M. Wang, S. Wei, Z. Zhou, J. Shi, and X. Zhang, "Efficient admm framework based on functional measurement model for mmw 3-d sar imaging," *IEEE Trans. Geosci. Remote Sens.*, vol. 60, pp. 1–17, 2022.

[23] G. Wang, F. Qi, Z. Liu, C. Liu, C. Xing, and W. Ning, "Comparison between back projection algorithm and range migration algorithm in terahertz imaging," *IEEE Access*, vol. 8, pp. 18 772–18 777, 2020.

[24] D. Sheen, D. McMakin, and T. Hall, "Three-dimensional millimeter-wave imaging for concealed weapon detection," *IEEE Transactions on Microwave Theory and Techniques*, vol. 49, no. 9, pp. 1581–1592, 2001.

[25] M. Wang, S. Wei, J. Liang, S. Liu, J. Shi, and X. Zhang, "Lightweight fista-inspired sparse reconstruction network for mmw 3-d holography," *IEEE Trans. Geosci. Remote Sens.*, vol. 60, pp. 1–20, 2022.

[26] Y. Rodríguez-Vaqueiro, Y. Álvarez López, B. González-Valdes, J. A. Martínez, F. Las-Heras, and C. M. Rappaport, "On the use of compressed sensing techniques for improving multistatic millimeter-wave portal-based personnel screening," *IEEE Trans. Antennas Propag.*, vol. 62, no. 1, pp. 494–499, 2014.

[27] S. Wu, L. Ding, P. Li, Y. Li, L. Chen, and Y. Zhu, "Millimeter-wave sar sparse imaging with 2-d spatially pseudorandom spiral-sampling pattern," *IEEE Trans. Microw. Theory Techn.*, vol. 68, no. 11, pp. 4672–4683, Nov. 2020.

[28] X. Zhuge and A. G. Yarovoy, "Study on two-dimensional sparse mimo uwb arrays for high resolution near-field imaging," *IEEE Transactions on Antennas and Propagation*, vol. 60, no. 9, pp. 4173–4182, 2012.

[29] Y. Zhang, Q. Yang, Y. Zeng, B. Deng, H. Wang, and Y. Qin, "High-quality interferometric inverse synthetic aperture radar imaging using deep convolutional networks," *Microw. Opt. Technol. Lett.*, vol. 62, no. 9, pp. 3060–3065, Jan. 2020.

[30] Q. Cheng, A. A. Ihalage, Y. Liu, and Y. Hao, "Compressive sensing radar imaging with convolutional neural networks," *IEEE Access*, vol. 8, pp. 212 917–212 926, Dec. 2020.

[31] J. Gao, B. Deng, Y. Qin, H. Wang, and X. Li, "Enhanced radar imaging using a complex-valued convolutional neural network," *IEEE Geosci. Remote Sens. Lett.*, vol. 16, no. 1, pp. 35–39, Jan. 2019.

[32] J.-F. Cai, E. J. Candès, and Z. Shen, "A singular value thresholding algorithm for matrix completion," *SIAM J. optim.*, vol. 20, no. 4, pp. 1956–1982, Mar. 2010.

[33] L. T. Nguyen, J. Kim, and B. Shim, "Low-rank matrix completion: A contemporary survey," *IEEE Access*, vol. 7, pp. 94 215–94 237, Jul. 2019.

[34] E. J. Candès, X. Li, Y. Ma, and J. Wright, "Robust principal component analysis?" *J. ACM*, vol. 58, no. 3, pp. 1–37, May 2011.

[35] D. Yang, G. Liao, S. Zhu, X. Yang, and X. Zhang, "Sar imaging with undersampled data via matrix completion," *IEEE Trans. Geosci. Remote Sens.*, vol. 11, no. 9, pp. 1539–1543, Sep. 2014.

[36] S. Zhang, G. Dong, and G. Kuang, "Matrix completion for downward-looking 3-d sar imaging with a random sparse linear array," *IEEE Trans. Geosci. Remote Sens.*, vol. 56, no. 4, pp. 1994–2006, Apr. 2018.

[37] S. Hu, C. Shu, Y. Alfadhl, X. Chen, and K. Wang, "Thz personnel screening system with multi-pass interferometric synthetic aperture technique," in *Proc. IEEE UK-Europe-China Workshop Milli. Waves and Terahz Technol.(UCMMT)*, Dec. 2020, pp. 1–3.

[38] G. Lockwood, P.-C. Li, M. O'Donnell, and F. Foster, "Optimizing the radiation pattern of sparse periodic linear arrays," *IEEE Trans. Ultrason., Ferroelectr, Freq. Control*, vol. 43, no. 1, pp. 7–14, 1996.

[39] S. Hu, C. Shu, Y. Alfadhl, and X. Chen, "A thz imaging system using linear sparse periodic array," *IEEE Sensors J.*, vol. 20, no. 6, pp. 3285–3292, Mar. 2019.

[40] E. J. Candès and T. Tao, "The power of convex relaxation: Near-optimal matrix completion," *IEEE Trans. Inf. Theory*, vol. 56, no. 5, pp. 2053–2080, May 2010.

[41] S. Patole and M. Torlak, "Two dimensional array imaging with beam steered data," *IEEE Trans. Image Process.*, vol. 22, no. 12, pp. 5181–5189, Sep. 2013.

[42] J. Wang and X. Liu, "Sar minimum-entropy autofocus using an adaptive-order polynomial model," *IEEE Geosci. Remote Sens. Lett.*, vol. 3, no. 4, pp. 512–516, 2006.

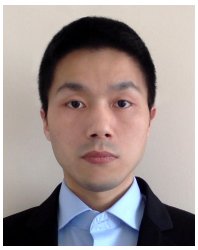

Shaoqing Hu (Member, IEEE) received the B.Eng. and M.Eng. degrees from the University of Electronic Science and Technology of China, Chengdu, Sichuan, China, in 2013 and 2016, and the Ph.D. degree from Queen Mary University of London, London, U.K., in 2020.

He is currently a lecturer with the Department of Electronic and Electrical Engineering, College of Engineering, Design & Physical Sciences, Brunel University London. He has authored or co-authored over 35 papers in international journals and conferences. His research interests include millimeter wave/THz security detection, sparse imaging, antennas, arrays, engineering optimisation and wireless communication.

Dr Hu was the Session Chair of APS/URSI 2020, TPC member of CNIS2023, ICVIP2021, ISAI 2017, ITA 2017. He is the recipient of Brunel University London Research Development Fund 2021 and BRIEF Award 2022/2023, Student Paper Award with IEEE Asia-Pacific Conference on Antennas and Propagation in 2015, and First Prize of Best Student Paper Award with UK-Europe-China Workshop on Millimeter Waves and THz Technologies in 2020. He is the member of IEEE, SPIE (The international society for optics and photonics) and working committee in UK of China Institute of Communications. He is the reviewer of many IEEE, IET, Hindawi and MDPI journals including IEEE Transactions on Geoscience and Remote Sensing, IEEE Transactions on Microwave Theory and Techniques, and IEEE Transactions on Instrumentation and Measurement.

Amir Masoud Molaei received the B.Sc. degree in communications engineering and the M.Sc. degree in telecommunication systems engineering from the Sahand University of Technology, Tabriz, Iran, in 2010 and 2013, respectively, and the Ph.D. degree in telecommunication systems engineering from the Babol Noshirvani University of Technology (BNUT), Babol, Iran, in 2019.

He is currently with the Centre for Wireless Innovation, School of Electronics, Electrical Engineering and Computer Science, Queen's University Belfast, as a Postdoctoral Research Fellow. During the period 2019–2020, he has joined Future Wave Ultratech Company as a Mobile Networks (GSM/UMTS/LTE) Analyzer and Planner. From 2015 to 2019, he was a Lecturer with the Faculty of Electrical Engineering, BNUT; the Mazandaran Institute of Technology; and Islamic Azad University. He was ranked first in the Ph.D. entrance exam in telecommunication systems at BNUT and ranked first among the Ph.D. graduates from the Telecommunication Engineering Department. He has published over 35 refereed papers and has filed two patents. His current research interests include signal processing, radar imaging algorithms, and sensor arrays.

Dr. Molaei is the General Chair of the 2022 International Conference on Manufacturing, Industrial Automation and Electronics (ICMIAE 2022). He has served as a Senior Editor for the Cloud Computing and Data Science (CCDS). He has also served as a Technical Reviewer for numerous prestigious leading journals, including IEEE Wireless Communications, IEEE Transactions on Automation Science and Engineering, and IEEE Transactions on Vehicular Technology

Okan Yurduseven (Senior Member, IEEE) received the Ph.D. degree in electrical engineering from Northumbria University, Newcastle upon Tyne, United Kingdom in 2014.

He is currently a Reader (Associate Professor) at the School of Electronics, Electrical Engineering and Computer Science, Queen's University Belfast, UK. Prior to this, he was a NASA Research Fellow at the NASA Jet Propulsion Laboratory, California Institute of Technology, USA. He is also an Adjunct Professor at Duke University, USA. His research interests include microwave and millimeter-wave imaging, multiple-input-multiple-output (MIMO) radars, wireless power transfer, antennas and propagation and metamaterials. He has authored more than 150 peer-reviewed technical journal and conference articles, and has been Principal Investigator & Co-Investigator on research grants totaling in excess of £10M in these fields.

Dr Yurduseven is the recipient of several awards, including an Outstanding Postdoc at Duke University Award (2017), Duke University Professional Development Award (2017), NASA Postdoctoral Program Award (2018), British Council - Alliance Hubert Curien Award (2019), Leverhulme Trust Research Leadership Award (2020), Young Scientist Award from the Electromagnetics Academy - Photonics and Electromagnetics Research Symposium (2021) and the Queen's University Belfast Vice Chancellor's Early Career Researcher Prize (2022). He serves as an Associate Editor of the IEEE Antennas and Wireless Propagation Letters, Nature Scientific Reports and MDPI Remote Sensing. He is a member of the European Association on Antennas and Propagation (EurAAP).

Hongying Meng (Senior Member, IEEE) received his PhD degree in Communication and Electronic Systems from Xi'an Jiaotong University, Xi'an China. He is an associate editor for IEEE Transactions on Circuits and Systems for Videos Technology (TCSVT) and IEEE Transactions on Cognitive and Developmental Systems (TCDS). He has authored over 160 publications including IEEE TIP, TCYB, TFS, TAC, TCSVT, TBE, TCDS, ICASSP and CVPR. He is currently a Reader at the Department of Electronic and Electrical Computer Engineering, Brunel University London, U.K. His research interests include digital signal processing, effective computing, machine learning, human computer interaction, and computer vision.

Rajagopal Nilavalan (Senior Member, IEEE) received the B.Sc. Eng degree in electrical and electronics engineering from the University of Peradeniya, Sri Lanka, in 1995 and the PhD degree in radio frequency systems from the University of Bristol, Bristol, U.K., in 2001. From 1999 to 2005, he was a Researcher at the Centre for Communications Research (CCR) at the University of Bristol, U.K. At Bristol, his research involved theoretical and practical analyses of postreception synthetic focusing concepts for near-field imaging and research on numerical FDTD techniques. Since 2005, he has been with the Department of Electronics and Computer Engineering, Brunel University, U.K., where he is currently a Senior Lecturer in wireless communications. His main research interests include antennas and propagation, microwave circuit designs, numerical electromagnetic modeling, and wireless communication systems. He has published over 100 papers and articles in journals and international conferences in his research area.,Dr. Nilavalan was a member of the European commission, Network of Excellence on Antennas from 2002 to 2005 and a member of the IET.

Lu Gan (Senior Member, IEEE) received the B.Eng. and M.Eng. degrees from South East University, Nanjing, China, and the Ph.D. degree from Nanyang Technological University, Singapore, in 1998, 2000, and 2004, respectively. She is currently a Senior Lecturer (equivalent to Associate Professor) with Brunel University London, London, U.K.. She has been on the faculties of the University of Newcastle, Callaghan, NSW, Australia, from 2004 to 2006, and University of Liverpool, Liverpool, U.K., from 2006 to 2007. Her research interests include fundamental signal processing theories and their applications in image/video coding and processing, nondestructive terahertz and ultrasound imaging, machine learning, and wireless communications. Dr. Gan was the Technical Committee Member for conferences including ICASSP, ICIP, Globecom, and ICC. She is a reviewer for research grants of EPSRC, STFC, FWO and many top journals including IEEE Transactions on Information Theory, IEEE Transactions on Signal Processing, IEEE Transactions on Communications, and IEEE Transactions on Image Processing. She serves as an Associate Editor for the IEEE Signal Processing Letters.

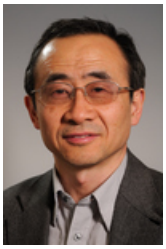

Xiaodong Chen (Fellow, IEEE) received the B.Sc. degree in electronics engineering from the University of Zhejiang, Hangzhou, China, in 1983, and the Ph.D. degree in microwave electronics from the University of Electronic Science and Technology of China, Chengdu, China, in 1988.

He joined the Department of Electronic Engineering, King's College, University of London, London, U.K., in 1988, as a Postdoctoral Visiting Fellow. In 1990, he was employed by the King's College as a Research Associate and was appointed to a lectureship later on. In 1999, he joined the School of Electronic Engineering and Computer Science, Queen Mary University of London, London, where he is currently a Professor of Microwave Engineering with the School of Electronic Engineering and Computer Science. He has authored or coauthored over 400 publications (book chapters, journal articles, and refereed conference presentations). His current research interests include high-power microwave devices, wireless communications, and antennas.

Dr Chen is a member of the U.K. Engineering and Physical Sciences Research Council Review College and the Technical Panel of the Institution of Engineering and Technology Antennas and Propagation Professional Network. He is a Fellow of IET/IEEE.